

5. J. R. Heath, M. A. Ratner, *Phys. Today* **2003**, 43 (May 2003).
6. N. Seeman, *Nature* **421**, 427 (2003).
7. C. A. Mirkin, R. L. Letsinger, R. C. Mucic, J. J. Storhoff, *Nature* **382**, 607 (1996).
8. A. P. Alivisatos *et al.*, *Nature* **382**, 609 (1996).
9. E. Winfree, F. Liu, L. A. Wenzler, N. C. Seeman, *Nature* **394**, 539 (1998).
10. C. Niemeyer, *Curr. Opin. Chem. Biol.* **4**, 609 (2000).
11. E. Braun, Y. Eichen, U. Sivan, G. Ben-Yoseph, *Nature* **391**, 775 (1998).
12. Y. Eichen, E. Braun, U. Sivan, G. Ben-Yoseph, *Acta Polym.* **49**, 663 (1998).
13. K. Keren *et al.*, *Science* **297**, 72 (2002).
14. K. A. Williams, P. T. M. Veenhuizen, B. G. de la Torre, R. Eritja, C. Dekker, *Nature* **420**, 761 (2002).
15. F. Balavoine *et al.*, *Angew. Chem. Int. Ed.* **38**, 1912 (1999).
16. M. Shim, N. W. S. Kam, R. J. Chen, Y. Li, H. Dai, *Nano Letters* **2**(4), 285 (2002).
17. G. R. Dieckmann *et al.*, *J. Am. Chem. Soc.* **125**, 1770 (2003).
18. D. Pantarotto *et al.*, *J. Am. Chem. Soc.* **125**, 6160 (2003).
19. M. M. Cox, *Prog. Nucleic Acid Res. Mol. Biol.* **63**, 311 (2000).
20. Materials and Methods are available as supporting online material on Science Online.
21. J. Liu *et al.*, *Science* **280**, 1253 (1998).
22. C. Gomez-Navarro *et al.*, *Proc. Natl. Acad. Sci. U.S.A.* **99**, 8484 (2002).
23. M. Bockrath *et al.*, *Nano Letters* **2**, 187 (2002).
24. P. Avouris, *Acc. Chem. Res.* **35**, 1026 (2002).
25. K. Bradley, J. Cumings, A. Star, J. C. P. Gabriel, G. Grulner, *Nano Letters* **3**, 639 (2003).
26. R. Krupke, F. Hennrich, H. v. Lohneysen, M. M. Kappes, *Science* **301**, 344 (2003).
27. D. Chattopadhyay, I. Galeska, F. Papadimitrakopoulos, *J. Am. Chem. Soc.* **125**, 3370 (2003).
28. M. Zheng *et al.*, *Nature Mater.* **2**, 338 (2003).

29. We thank C. Dekker and K. Williams for helpful discussions regarding the attachment of streptavidin to nanotubes and for providing us with purified nanotube material suspended in SDS. We thank M. Konorty, Y. Cohen, Y. Dror, U. Banin, and Y. Ebenstein for help and discussions and N. Brenner for comments on the manuscript. The research was conducted in the Ben and Esther Rosenbloom Nanoelectronics by Biotechnology center of excellence. Research was supported by the Israeli Science Foundation and the Technion grant for promotion of research. K.K. acknowledges support by the Clore Foundation.

Supporting Online Material

www.sciencemag.org/cgi/content/full/302/5649/1380/DC1

Materials and Methods

Figs. S1 to S4

References

2 September 2003; accepted 15 October 2003

An Atomic-Level View of Melting Using Femtosecond Electron Diffraction

Bradley J. Siwick, Jason R. Dwyer, Robert E. Jordan, R. J. Dwayne Miller

We used 600-femtosecond electron pulses to study the structural evolution of aluminum as it underwent an ultrafast laser-induced solid-liquid phase transition. Real-time observations showed the loss of long-range order that was present in the crystalline phase and the emergence of the liquid structure where only short-range atomic correlations were present; this transition occurred in 3.5 picoseconds for thin-film aluminum with an excitation fluence of 70 millijoules per square centimeter. The sensitivity and time resolution were sufficient to capture the time-dependent pair correlation function as the system evolved from the solid to the liquid state. These observations provide an atomic-level description of the melting process, in which the dynamics are best understood as a thermal phase transition under strongly driven conditions.

Solid-liquid phase transitions are an everyday occurrence. As one of the state variables (such as temperature or pressure) approaches a phase transition point for the melting of a solid, there are equilibrium fluctuations that lead to density changes commensurate with the new phase. Fluctuations important to a collective phase transition under these conditions occur over distributed time and length scales in which the atomic details are washed out. By using short-pulsed lasers to deposit heat at a rate faster than the thermal expansion rate, it is possible to prepare extreme states of solid matter at temperatures well above the normal melting point (this will be referred to as the strongly driven limit). Under such conditions, the atomic configuration of the entire excited material volume can be modified on the ultrafast time scale, and the melting transition of the prepared state can be seen as a simple model for transition state processes in general.

An atomistic view of such a process requires that the atomic configuration of the material be observed as it passes from the solid to the liquid state. Ideally, one would like to be able to fully resolve the relative atomic motions during the melting process. The information accessible through time-resolved diffraction experiments, where the observable is intimately connected with the atomic structure of the material (*1*), can approach such a description. The first experiment along these lines used electron diffraction combined with rapid laser heating, but lacked sufficient temporal resolution (20 to 100 ps) and structural sensitivity for an atomic-level perspective on the process (*2*). Important applications of time-resolved electron diffraction have recently provided atomic-level structural details of reactive intermediates in the gas phase occurring on a similar time scale (*3–5*). Approaches based on laser-driven x-ray plasma sources have provided improved temporal resolution (200 to 500 fs) but to date have an insufficient signal-to-noise ratio (structural sensitivity) to adequately resolve the atomic details (*6–8*). Here we describe an important advance

in short-pulsed electron sources that has made it possible to attain femtosecond electron pulses with sufficient electron number density to study the structural evolution of aluminum (Al) as it undergoes an ultrafast laser-induced solid-liquid phase transition. This work gives an atomic-level perspective on one of the simplest transition state processes: the order-to-disorder phase transition involved in melting.

Previous studies of femtosecond laser irradiation of polycrystalline Al at high fluence have observed the onset of liquid-like dielectric properties within 500 fs after laser excitation (*9*). It was inferred that lattice melting had occurred on this time scale, which is shorter than the time required for the optically excited electrons in the solid to relax via lattice phonon scattering. A nonthermal mechanism for melting was thus proposed, wherein the lattice bonding softens because of the photoinduced changes in electron distribution. Similar observations have been made in other materials (*10, 11*); however, it is not possible to determine detailed quantitative information about the nuclear coordinates from the electronic response (probed in optical measurements), especially for these far-from-equilibrium conditions. Time-resolved diffraction offers a direct probe of the atomic structure of polycrystalline and amorphous samples by providing, through a simple transformation, the time-dependent (atomic) pair correlation function. Such a measurement is able to determine how the lattice structure maps onto the disordered state defining a liquid. In the case of Al, we were able to follow the loss of the long-range order that was present in the crystalline phase and the emergence of the liquid structure where only short-range atomic correlations were present; the transition was complete within 3.5 ps for 20-nm-thick samples at an excitation fluence of 70 mJ/cm². As opposed to previous studies of strongly driven phase transitions, we were able to define the onset of the liquid state and found that even in the strong perturbation limit, the phase transition in Al is propagated by thermally sampled

Departments of Chemistry and Physics, 80 St. George Street, University of Toronto, Toronto, Ontario, Canada M5S 3H6.

configurations, albeit in a superheated metastable state: The solid shakes itself apart.

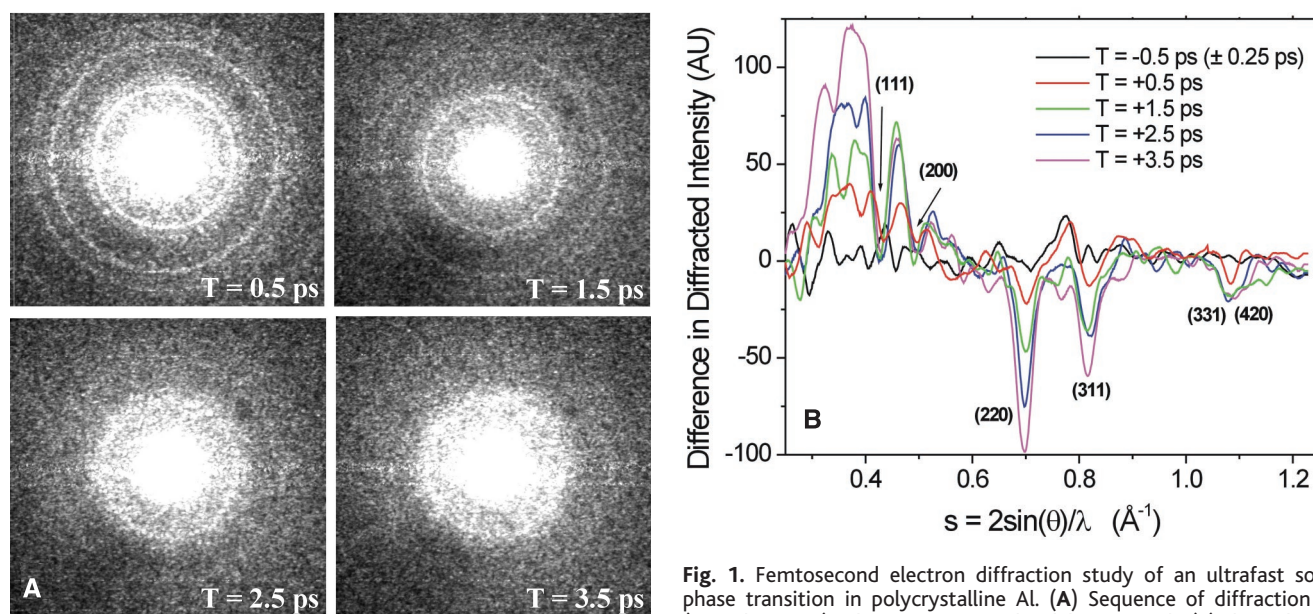
To study the changes in atomic configuration accompanying the transition, we performed pump-probe transmission electron diffraction measurements on polycrystalline Al films that were 20 ± 2 nm thick (12). Previous efforts to achieve subpicosecond temporal resolution with electron pulses containing the number density required in these studies have experienced degradation to the picosecond domain by space-charge (Coulomb repulsion) broadening effects during pulse propagation (13) and/or geometric broadening of the time resolution by velocity mismatch between optical and electron pulses over sample volumes (14, 15). The latter is not an issue for 20-nm-thick solid-state samples. Detailed simulation of space-charge-induced pulse broadening, the results of which are presented elsewhere (16), was used to design a photoactivated electron gun capable of delivering sub-500-fs electron pulses (fig. S2B) containing number densities sufficient for structure determinations with fewer than 100 shots (17). The femtosecond electron diffractometer consists primarily of the femtosecond laser-driven 30-keV electron source, a sample positioning system and microchannel plate-phosphor screen detector contained in a high-vacuum chamber, and an external, lens-coupled, charge-coupled device camera to image the diffraction patterns. As configured for these experiments, the detector collected scattering vectors (s) up to a

magnitude of $s = 2\sin(\theta)/\lambda = 1.35 \text{ \AA}^{-1}$. This range of diffraction angles encompasses the first 10 rings of the powder diffraction pattern of Al (18). Excellent signal-to-noise diffraction patterns were obtained with 150 shots, using electron pulses of 600 ± 100 fs (6000 ± 500 electrons per pulse). The high quality of the data demonstrates the benefit of both the large elastic scattering cross-section of electrons (8) and their relatively high efficiency of detection.

The phase transition was driven with 120-fs near-infrared (775 nm) laser pulses, 70 mJ/cm² fluence, which is well above the reported threshold for nonthermal melting in Al (9). Diffraction patterns were recorded at pump-probe delay intervals of 500 fs near the time origin until the onset of the solid-liquid phase transition, and at coarser time steps thereafter. The results of this experiment are shown in Fig. 1. By 3.5 ps, the structure of the diffraction pattern has changed completely from the sequence of rings that is characteristic of the face-centered cubic (fcc) structure of polycrystalline Al, to a liquid-like pattern with only a single broad ring visible (Fig. 1A). The dynamics of the phase transition are further highlighted by taking the radial average of the difference in diffracted intensity, with respect to that of the unperturbed structure, at each time delay (Fig. 1B). In less than 1.5 ps, the diffraction rings indexed to the (331) and (420) lattice planes are no longer observable, whereas the (220) and (311) rings have been reduced in intensity by

45 and 60%, respectively. The decay time of the diffraction features has a strong s dependence—a signature of thermal excitation. Displacements of Al atoms from their equilibrium positions due to thermal motion diminish the ring intensities by the Debye-Waller factor e^{-2M} , where M depends on the mean square atomic displacements (a function of temperature) and s^2 (19). The observed melting dynamics are significantly slower than that inferred from dielectric function measurements (9) and can be understood within the confines of a thermal disordering process.

The 3.5-ps time scale is effectively set by the magnitude of the electron-phonon coupling constant in Al and makes electronically driven disordering unlikely. Based on the fast electron redistribution times in metals (20) and the thermalization rate of the hot electron energy redistribution into lattice phonons (21), the Al lattice is expected to achieve the melting point temperature ($T_M = 933$ K) within 750 fs after excitation under the strongly driven condition of this experiment (22). This corresponds to a heating rate of more than 800 K/ps. By 1.5 ps, the projected lattice temperature T_1 is 1400 K ($T_1/T_M \sim 1.5$), which suggests significant superheating during the phase transition. This superheated phase of Al is highly unstable (23–25) and exists only transiently. Within 3.5 ps, the lattice has disordered to such a degree that the diffraction peaks associated with all lattice planes have been reduced to below the noise



transition. The first four rings in the powder diffraction pattern, associated with the fcc lattice structure, are still clearly visible 500 fs after laser excitation. At $T = 3.5$ ps, features associated with Bragg reflections are no longer visible, and the diffraction pattern exhibits only a single broad ring, which is characteristic of a liquid. Each diffraction pattern contains the cumulative diffracted intensity of only 150 electron pulses. (B) Radial average of the difference in diffracted intensity, with respect to that of the unperturbed crystalline state (that is, before the phase transition) at each time delay (AU, arbitrary units). The decay time of the diffraction rings has a strong dependence on the scattering vector s , which is characteristic of thermal excitation. The loss of long-range order associated with the phase transition is best seen in the dramatic broadening of the (111) and (200) diffraction ring feature in the $s < 0.4$ region, not simply in the reduction in ring intensities, because they are strongly temperature-dependent.

REPORTS

level of these measurements. The absence of discrete features (lines) associated with Bragg reflections in the diffraction pattern reveals the complete loss of long-range order: The solid has truly melted. There is no observable shift in the position of the diffraction peaks. This indicates the absence of significant lattice expansion during the transition.

A recent model of laser-driven solid-liquid phase transitions based on the propagation of solid-liquid melt zones predicts faster dynamics than those observed for Al without invoking nonthermal mechanisms under these conditions (24). The calculated response depends on material parameters, such as interfacial surface tension, that are not well defined at these elevated conditions. It will be informative to test the general validity of this homogeneous nucleation model by comparing different solids.

To gain an atomic perspective on the melting process and better quantify the material response, the information contained in the diffraction patterns of polycrystalline and amorphous samples can be reexpressed in terms of an average pair correlation function, $H(r)$, by a sine transform of the reduced diffracted intensity (18, 26)

$$H(r) = 4\pi r^2 \left[\rho(r) - \rho_0 \right] \\ = 8\pi r \int_0^\infty s \left[K(s) - 1 \right] \sin(2\pi sr) ds \quad (1)$$

where the structure factor $K(s) = I(s)/f^2(s)$. $I(s)$ is the coherently diffracted intensity in electron units (27), $f(s)$ is the atomic scattering factor (28), $\rho(r)$ is the atomic density, and ρ_0 is the average atomic density. $H(r)$, often called the reduced radial density function, describes the deviation in atomic density from the average value as a function of the radial distance r from an atomic origin. This analysis was performed on high-quality diffracted intensity curves (accumulated from 1200 electron pulses) at time delays (T) of -1, +6, and +50 ps. The results are presented in Fig. 2, from which the nature of the structural transformation in terms of pair correlations becomes clear. Before the phase transition (-1 ps), the diffraction spectrum consists of a set of discrete lines (Fig. 2A), each of which can be referred to by the Miller index of the particular set of lattice planes that give rise to that reflection. $H(r)$ shows significant structure, and the long-range correlations in atomic position that exist before the phase transition are evident (Fig. 2B). The peaks in $H(r)$ correspond to distances between pairs of atoms in the fcc structure of Al [except the first peak, which is spurious and due to the effects of terminating the measured data at $s = 1.35 \text{ \AA}^{-1}$ (18)] and have positions accurate to within $\pm 0.05 \text{ \AA}$. The ultrafast transition from the solid to the liquid state is clear from $H(r)$ obtained at 6 ps after the laser excitation. Long-range order has been completely lost, and only short-range correlations in atomic position survive. The simple shell structure of liquids is apparent in $H(r)$, which has lost the higher frequency oscillations associated with

the fcc structure of the crystalline state. We were able to determine the positions of the first three coordination shells [r_1 (+6 ps) = $2.85 \pm 0.05 \text{ \AA}$, r_2 (+6 ps) = $4.9 \pm 0.1 \text{ \AA}$, and r_3 (+6 ps) = $7.6 \pm 0.1 \text{ \AA}$], and they are in approximate agreement with values obtained from x-ray diffraction studies of liquid Al ($r_1 = 2.9 \pm 0.1 \text{ \AA}$, $r_2 = 5.2 \pm 0.1 \text{ \AA}$, and $r_3 = 7.6 \pm 0.1 \text{ \AA}$) (18). There are subtle changes on longer time scales as well, as the width of the main peak in the structure factor broadens toward lower scattering vectors from 6 to 50 ps. This width is inversely related to the length scale over which atomic positions are correlated and has a clear impact on $H(r)$. There is a significant reduction in the height of the second peak at $r \sim 5 \text{ \AA}$, which has shifted slightly to r_2 (+50 ps) = $5.1 \pm 0.1 \text{ \AA}$ to better match the position reported for liquid Al. In fact, all peaks in $H(r)$ appear to shift slightly to larger distance between 6 and 50 ps. These observations suggest that the liquid structure has not fully equilibrated by 6 ps and that the disordered structure observed is influenced by correlations that exist in the crystalline state. Peak positions in $H(r)$, unlike amplitudes, appear to be quite insensitive to temperature (18); however, we are not aware of a study on liquid Al at the expected final temperature of these studies ($\sim 1200 \text{ K}$ according to a thermodynamic calculation). It is difficult, therefore, to say whether the structure at 50 ps has reached the equilibrium atomic configuration.

From $H(r)$ and the average density of the material (29), we were able to determine the changes in the first coordination number (N_1)

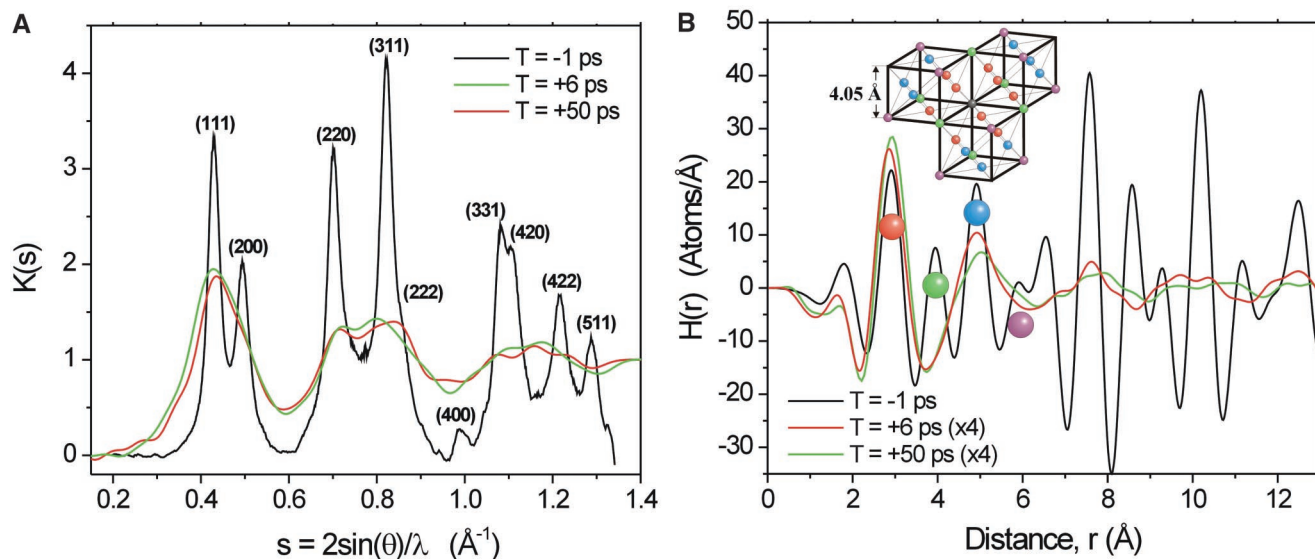


Fig. 2. Snapshots of the time-dependent pair correlation function. (A) Comparison of the structure factor $K(s)$ at pump-probe delays before and after the phase transition. These curves were obtained from diffraction patterns containing the cumulative diffracted intensity of 1200 electron pulses. (B) Radial density functions, $H(r)$, computed from the measured structure factors shown. The $T = +6$ and $+50$ ps curves have been scaled by a factor of 4 to better show the structure. The correspondence between the peaks in $H(r)$ at $T = -1$ ps and the interatomic spacings present in the fcc Al lattice (inset) are

shown for the first four peaks. Atoms of a given color are the same distance from the central black atom. The peak in $H(r)$ that each interatomic separation produces is labeled with a circle of the same color. Only short-range correlations in atomic position are present at $T = +6$ ps, and the highly modulated structure of $H(r)$ that is due to the fcc lattice is replaced by the simple coordination shell structure of liquids. Subtle changes occur between 6 and 50 ps; namely, a shift in the correlation peaks to larger distance and a significant reduction in the magnitude of the second peak at $r \sim 5 \text{ \AA}$.

that accompany the phase transition. Before the phase transition (-1 ps), we calculated N_1 to be 12.2 ± 0.3 , which, within error, is the expected number for an fcc lattice (12). The loss of lattice structure and the subsequent atomic rearrangements reduce N_1 to 10.0 ± 0.3 at 6 ps. There is no observable change on longer time scales, as $N_1 = 10.0 \pm 0.3$ at 50 ps as well.

The new technique of femtosecond electron diffraction has provided an unprecedented atomic-level view of ultrafast solid-liquid phase transition dynamics. In this instance, the picture it provides can be expressed in terms of an average pair correlation function, $H(r)$, which contains detailed information on nearest-neighbor distances, coordination numbers, and mean square vibrational amplitudes of the non-equilibrium state at each instant during the transition. This is a general technique, however, and can be applied to myriad systems in which photoinduced structural dynamics occur on the femtosecond time scale. Excellent candidates for investigation include condensed-phase processes, surface chemistry, and even time-resolved protein crystallography in cases where electron diffraction is viable. The single most important achievement is that of subpicosecond time resolution with sufficient structural sensitivity to reveal the atomic details of even nonreversible transition state processes that are central to concepts in chemistry and biology.

References and Notes

- A. Guinier, *X-Ray Diffraction in Crystals, Imperfect Crystals and Amorphous Bodies* (Dover, New York, 1994).
- S. Williamson, G. Mourou, J. C. M. Li, *Phys. Rev. Lett.* **52**, 2364 (1984).
- V. A. Lobastov *et al.*, *J. Phys. Chem. A* **105**, 11159 (2001).
- H. Ihee *et al.*, *Science* **291**, 458 (2001).
- R. C. Dudek, P. M. Weber, *J. Phys. Chem. A* **105**, 4167 (2001).
- A. Rousse *et al.*, *Nature* **410**, 65 (2001).
- K. Sokolowski-Tinten *et al.*, *Phys. Rev. Lett.* **87**, 225701 (2001).
- The key advantage of using electron diffraction for such investigations is the 10^5 to 10^6 enhancement in scattering cross-section as compared with x-rays. The result is that the mean free path for elastic scattering of electrons (~ 25 nm for 30-keV electrons through Al) is nearly perfectly matched with the excitation volume in studies of laser-induced phase transitions, which is inherently limited to several times the optical penetration depth.
- C. Guo, G. Rodriguez, A. Lobad, A. J. Taylor, *Phys. Rev. Lett.* **84**, 4493 (2000).
- C. V. Shank, R. Yen, C. Hirlimann, *Phys. Rev. Lett.* **50**, 454 (1983).
- J. P. Callan, A. M. T. Kim, L. Huang, E. Mazur, *Chem. Phys.* **251**, 167 (2000).
- Materials and methods are available as supporting material on Science Online.
- J. Cao *et al.*, *Appl. Phys. Lett.* **83**, 1044 (2003).
- J. C. Williamson, J. Cao, H. Ihee, H. Frey, A. H. Zewail, *Nature* **386**, 159 (1997).
- J. C. Williamson, A. H. Zewail, *Chem. Phys. Lett.* **209**, 10 (1993).
- B. J. Siwick, J. R. Dwyer, R. E. Jordan, R. J. D. Miller, *J. Appl. Phys.* **92**, 1643 (2002).
- The electron pulse duration (at the sample) is strongly dependent on the number of electrons in the pulse and on the beam diameter. Pulses containing 6000 ± 500 electrons, as used in these experiments, have a duration of 600 ± 100 fs at the sample, whereas pulses containing 3000 ± 500 electrons have a duration of only 450 ± 50 fs.
- R. R. Fessler, R. Kaplow, B. L. Averbach, *Phys. Rev.* **150**, 34 (1966).
- R. W. James, *The Optical Principles of the Diffraction of X-rays* (Bell, London, 1962), chap. 5.
- C. A. Schmuttenmaer *et al.*, *Phys. Rev. B* **50**, 8957 (1994).
- R. Rethfeld, A. Kaiser, M. Vicanek, G. Simon, *Phys. Rev. B* **65**, 214303 (2002).
- The expected lattice temperatures are calculated using the two-temperature model (TTM) described in (27). The material parameters that enter the TTM are the electron heat capacity coefficient $\gamma = 125$ J/m³K (from which the electron heat capacity $C_e = \gamma T_e$ is determined); the lattice heat capacity $C_l = 2.4 \times 10^6$ J/m³K; and the electron-phonon coupling constant $g = 3.1 \times 10^{17}$ W/m³K [from (27)].
- S. N. Luo, T. J. Ahrens, *Appl. Phys. Lett.* **82**, 1836 (2003).
- R. Rethfeld, K. Sokolowski-Tinten, D. von der Linde, S. I. Anisimov, *Phys. Rev. B* **65**, 092103 (2002).
- Z. H. Jin, P. Gumbsch, K. Lu, E. Ma, *Phys. Rev. Lett.* **87**, 055703 (2001).
- D. J. H. Cockayne, D. R. McKenzie, *Acta Crystallogr.* **A44**, 870 (1988).
- To convert the measured $I(s)$ to electron units requires a normalization constant, N , to be determined. We used a standard procedure that makes use of the high-angle fitting criterion to perform an initial determination of N , and then fine-tuned this value by minimizing oscillations near $r \approx 0$ Å in the calculated $H(r)$. Further discussion of this procedure, and errors associated with the incorrect determination of N , can be found in (18, 26) and references contained therein.
- P. A. Doyle, P. S. Turner, *Acta Crystallogr.* **A24**, 390 (1968).
- The average density in all cases was taken to be that of solid Al, $\rho_0 = 0.06021$ atoms/Å³. Because the phase transition will result in a decrease in ρ_0 (the density of solid Al is approximately 6% higher than that of liquid Al), the N_1 values determined at 6 and 50 ps are likely overestimated by a few percent.
- Supported by the Canada Foundation for Innovation, the Ontario Innovation Trust, the Natural Sciences and Engineering Research Council of Canada, and the Connaught Fund. J.R.D. gratefully acknowledges the support of a Walter C. Sumner fellowship.

Supporting Online Material

www.sciencemag.org/cgi/content/full/302/5649/1382/DC1

Materials and Methods
Figs. S1 and S2

References

4 August 2003; accepted 10 October 2003

Impacts of Fine Root Turnover on Forest NPP and Soil C Sequestration Potential

Roser Matamala,^{1*} Miquel A. González-Meler,² Julie D. Jastrow,¹ Richard J. Norby,³ William H. Schlesinger⁴

Estimates of forest net primary production (NPP) demand accurate estimates of root production and turnover. We assessed root turnover with the use of an isotope tracer in two forest free-air carbon dioxide enrichment experiments. Growth at elevated carbon dioxide did not accelerate root turnover in either the pine or the hardwood forest. Turnover of fine root carbon varied from 1.2 to 9 years, depending on root diameter and dominant tree species. These long turnover times suggest that root production and turnover in forests have been overestimated and that sequestration of anthropogenic atmospheric carbon in forest soils may be lower than currently estimated.

Roots provide a path for movement of carbon and energy from plant canopies to soils; thus, root production and turnover directly impact the biogeochemical cycle of carbon in terrestrial ecosystems. However, accurate estimates of root life-spans and turnover rates have been elusive, and the impacts of root turnover on belowground processes in terrestrial ecosystems are not well known (1). Uncertainties in estimates of root longevity pre-

vent proper quantification of net primary productivity (NPP) and belowground C allocation in forests. The contribution of root C to the formation of soil organic matter depends on root productivity, turnover rates, exudation, mycorrhizal colonization, and soil characteristics, all of which vary with forest type. Current estimates have indicated that fine root production contributes from 33 to 67% (2–4) of the annual NPP in forest ecosystems. These estimates assumed root turnover rates of about 1 year, despite reported turnover rates ranging from days to several years (1). Estimates of root turnover and longevity have been obtained through conventional biomass assessments (4, 5), nitrogen budgeting (6), direct observation in minirhizotrons (7), pulse-labeling experiments using ¹⁴C- (8) or ¹⁵N-enriched fertilizers (9), and measurements of bomb-derived radiocarbon in root

¹Environmental Research Division, Argonne National Laboratory, Argonne, IL 60439, USA. ²Department of Biological Sciences, University of Illinois at Chicago (UIC), Chicago, IL 60607, USA. ³Environmental Sciences Division, Oak Ridge National Laboratory (ORNL), Oak Ridge, TN 37831, USA. ⁴Nicholas School of Environment and Earth Sciences, Duke University, Durham, NC 27708, USA.

*To whom correspondence should be addressed. E-mail: matamala@anl.gov